

# Collective response of nuclei : comparison between experiments and extended mean-field calculations

Denis Lacroix<sup>a)</sup>, Sakir Ayik<sup>b)</sup> and Philippe Chomaz<sup>c)</sup>

<sup>a)</sup> *LPC/ISMRA, Blvd du Maréchal Juin, 14050 Caen, France*

<sup>b)</sup> *Tennessee Technological University, Cookeville TN38505, USA*

<sup>c)</sup> *G.A.N.I.L., B.P. 5027, F-14076 Caen Cedex 5, France*

## Abstract

The giant monopole, dipole and quadrupole responses in  $^{40}\text{Ca}$ ,  $^{90}\text{Zr}$ ,  $^{120}\text{Sn}$  and  $^{208}\text{Pb}$  are investigated using linear response treatment based on a stochastic one-body transport theory. Effects of the coupling to low-lying surface modes (coherent mechanism) and the incoherent mechanism due to nucleon-nucleon collisions are included beyond the usual mean-field description. We emphasize the importance of both mechanism in the fragmentation and damping of giant resonance. Calculated spectra are compared with experiment in terms of percentage of Energy-Weighted Sum-Rules in various energy regions. We obtained reasonable agreement in all cases. A special attention has been given to the fragmentation of the Giant Quadrupole Resonance in calcium and lead. In particular, the equal splitting of the  $2^+$  in  $^{40}\text{Ca}$  is correctly reproduced. In addition, the appearance of fine structure in the response  $^{208}\text{Pb}$  is partly described by the calculations in which the coherent mechanism play an important role.

(November 6, 2018)

**PACS:** 24.30.Cz, 21.60.Jz, 25.70.Lm

**Keywords:** extended TDHF, linear response, one-body transport theory.

## I. INTRODUCTION

Recent development of high resolution experiments offers the possibility for a deeper understanding of collective motion in quantum fermionic system like nuclei. These experiments enable to determine the fragmentation of the nuclear response with a very high resolution up to few keV [1–4]. Understanding of the fine structure in the nuclear collective response, its fragmentation and damping mechanisms constitute a major challenge for theoretical models [5–8]. One possible avenue is the development of quantum transport theories for nuclear dynamics [9,10].

In dynamics of nuclear motion, one usually distinguishes damping due to the coupling to the external and the internal degrees of freedom. The former one gives rise to cooling of the system by evaporation of particles, while the latter one leads to the dispersion of the well ordered motion through mixing with the internal degrees of freedom. In the latter case, one can again distinguish (i) the Landau damping due to spreading of the collective modes over non-collective particle-hole (p-h) excitation, (ii) the coherent mechanism due to coupling with low-lying surface modes [5,11], and (iii) the damping due to coupling with the incoherent 2p-2h states usually referred to as the collisional damping [12,13].

Most investigations of the nuclear response carried out so far are based on either the coherent damping mechanism or the collisional damping. The coherent mechanism is, particularly, important at low temperature, and accounts for the main feature of fragmentation of the response [3,11,14–17]. On the other hand, the collisional damping is relatively weak at low temperature [18], but its magnitude becomes large with increasing temperature, as shown in recent calculations [19–22]. In this work, we carry out investigations of nuclear collective response on the basis of a one-body stochastic transport theory, which incorporates both the coherent mechanism and the collisional damping in an consistent manner as demonstrated in [23,24] (also see [25,26]). We calculate the giant monopole, dipole and quadrupole responses in  $^{40}\text{Ca}$ ,  $^{90}\text{Zr}$ ,  $^{120}\text{Sn}$  and  $^{208}\text{Pb}$ , and compare the results with experiment in terms of Energy-Weighted Sum-Rules distribution. We find that both mechanisms

play important role for a proper description of the fragmentation and the damping of giant resonance excitations.

In section II, we present a brief description of the linear response treatment of collective vibrations based the stochastic one-body transport theory . In section III, we discuss the details of the calculations and present the results and comparison with data in section IV. Finally, we give the conclusions in section V.

## II. LINEAR RESPONSE BASED ON STOCHASTIC TRANSPORT THEORY

### 1. Stochastic transport equation

In the stochastic transport theory, temporal evolution of the fluctuating single-particle density matrix  $\rho(t)$  is determined by [10],

$$i\hbar \frac{\partial}{\partial t} \rho(t) - [h(\rho), \rho(t)] = K_I(\rho) + \delta K(t) \quad (1)$$

where the left hand side corresponds to the mean-field evolution in terms of the self-consistent mean-field Hamiltonian  $h(\rho)$  expressed in terms of the fluctuating density, and the right hand side arises from the correlations due to residual interactions. The first term  $K_I(\rho)$ , which is usually referred to as the binary collision term, describes the coupling of single-particle excitations with more complicated two-particle two-hole states. It can be expressed as,

$$K_I(\rho) = \int_{t_0}^t [v, U_{12}(t, s) F_{12}(s) U_{12}^\dagger(t, s)] ds \quad (2)$$

where  $U_{12}(t, s)$  represents a product of the mean-field propagator  $U_{12} = U_1 \otimes U_2$  with  $U(t, s) = \exp\left(-i/\hbar \int_s^t h(\rho(t')) dt'\right)$  and

$$F_{12} = (1 - \rho_1)(1 - \rho_2)v\widetilde{\rho_1\rho_2} - \widetilde{\rho_1\rho_2}v(1 - \rho_1)(1 - \rho_2). \quad (3)$$

Here  $\widetilde{\rho_1\rho_2}$  Represents the anti-symmetric product of the single-particle density matrices and  $v$  denotes the residual interactions. As seen from eq.(2), the collision term, in general, involves memory effects due to the time integration over the past history from an initial

time  $t_0$  to the present time  $t$ . The second term in the right hand side of eq.(1) is the initial correlation term,

$$\delta K(\rho) = Tr_2[v, \delta\sigma_{12}(t)]. \quad (4)$$

where  $\delta\sigma_{12}(t) = U_{12}(t, t_0)\delta\sigma_{12}(t_0)U_{12}^\dagger(t, t_0)$  represents the propagation of the initial correlations from  $t_0$  to  $t$ . In the stochastic transport description, the initial correlations  $\delta\sigma_{12}(t)$  are treated as a Gaussian random quantity. Consequently, the initial correlation term  $\delta K(t)$  has a Gaussian distribution characterized by a zero mean and a second moment, which can be determined in accordance with the fluctuation-dissipation relation of the non-equilibrium statistical mechanics.

In the stochastic transport description, dynamical evolution is characterized by constructing an ensemble of solutions of the stochastic transport eq.(1). In this manner, the theory provides a basis for describing the average evolution, as well as, dynamics of density fluctuations. In the semi-classical approximation, a number of applications have been carried out for description of multi-fragmentation in heavy-ion collisions [27,28]. Furthermore, as demonstrated in recent publications [23,24], the stochastic evolution involves a coherent dissipation mechanism arising from the coupling of single-particle motion with the mean-field fluctuations. This can be shown by considering the average evolution of the single-particle density matrix  $\rho(t) = \bar{\rho}(t)$ . The ensemble average of eq.(1) is calculated by expressing the mean-field and the density matrix as  $h(\rho) = h(\bar{\rho}) + \delta h(t)$  and  $\rho(t) = \bar{\rho}(t) + \delta\rho(t)$ , where  $\delta h(t)$  and  $\delta\rho(t)$  represent the fluctuating parts of the mean-field and the density matrix, respectively. Then, the ensemble averaging yields a transport equation for the evolution of the average density matrix,

$$i\frac{\partial}{\partial t}\bar{\rho}(t) - [h(\bar{\rho}), \bar{\rho}(t)] = K_I(\bar{\rho}) + K_C(\bar{\rho}) \quad (5)$$

where  $K_I(\bar{\rho})$  represents the incoherent collision term and the additional term arises from the correlations of the mean-field fluctuations and the density fluctuations,

$$K_C(\bar{\rho}) = \overline{[\delta h(t), \delta\rho(t)]} \quad (6)$$

and it is referred to as the coherent collision term. For small fluctuations around the average evolution, the density fluctuations can be expressed in terms of RPA phonons, and the coherent term takes the form of a particle-phonon collision term. As a result, eq.(5) provides an extended mean-field description, which goes beyond the extended Time-Dependent Hartree-Fock theory by including a coherent collision term into the equation of motion in addition to the incoherent one <sup>1</sup>.

## *2. Linear response based of extended mean-field theory*

In this section, we consider the small amplitude limit the transport eq.(5) and give a brief description of the linear response formalism including both the incoherent and the coherent damping terms. A details description of the formalism can be found in recent publications [21,23].

The linear response of the system to an external perturbation can be described by considering the small amplitude limit of the transport eq.(5). The small deviations of the density matrix  $\delta\rho(t) = \rho(t) - \rho_0$  around a finite temperature equilibrium state  $\rho_0$  are determined by the linearized form of the transport eq.(5),

$$i\hbar\frac{\partial}{\partial t}\delta\rho - [h_0, \delta\rho] - [\delta U + A, \rho_0] = \delta K^I(\rho) + \delta K^C(\rho) \quad (7)$$

In this expression  $A(t) = A \exp(-i\tilde{\omega}t) + \text{h.c.}$  is a one-body harmonic excitation operator containing a small imaginary part  $\tilde{\omega} = \omega + i\eta$ , and  $\delta K_I(\rho)$  and  $\delta K_C(\rho)$  represents the linearized form of the non-Markovian incoherent and coherent collision terms, respectively.

The steady state solution of eq. (7) can be obtained by using a development in terms of the RPA functions,

$$\delta\rho(t) = [Q^+, \rho_0] \exp(-i\tilde{\omega}t) + \text{h.c.} \quad (8)$$

---

<sup>1</sup>In the following, we denote the average one-body density  $\bar{\rho}$  by  $\rho$ .

where  $Q^+ = \sum_{\lambda>0} z_\lambda^+ O_\lambda^\dagger - z_\lambda^- O_\lambda$ . In this expression,  $O_\lambda^\dagger$  and  $O_\lambda$  are the creation and annihilation operators of the RPA state  $\lambda$  of energy  $\hbar\omega_\lambda$ , which are determined by the finite temperature RPA equations [29],

$$\hbar\omega_\lambda O_\lambda^\dagger = [h_0, Q_\lambda^\dagger] + h_\lambda^\dagger, \quad (9)$$

where  $h_\lambda^\dagger = (\partial h / \partial \rho) \cdot \rho_\lambda^\dagger$ . Substituting the expression (8) into eq.(7) gives rise to a set of coupled equations for the amplitudes  $z_\lambda^+$  and  $z_\lambda^-$  coefficients that can be recast into a matrix form [21],

$$(\hbar\tilde{\omega} - \Sigma(\tilde{\omega})) \begin{pmatrix} z^+ \\ z^- \end{pmatrix} = \begin{pmatrix} A \\ -A^* \end{pmatrix} \quad (10)$$

where  $z^+$  and  $z^-$  are the amplitude vectors with components  $z_\lambda^+$  and  $z_\lambda^-$ ,  $A$  is the forcing vector with components  $A_\lambda = \text{Tr}[O_\lambda, A]\rho_0$  and  $\Sigma(\tilde{\omega})$  denotes the self-energy matrix. In the small amplitude limit, the self-energy can be separated into the incoherent part and the coherent part,  $\Sigma(\tilde{\omega}) = \Sigma_I(\tilde{\omega}) + \Sigma_C(\tilde{\omega})$ . According to [21], the expression of the incoherent part, which also contains the RPA energy, is given by

$$\Sigma_{\lambda\mu}^I(\tilde{\omega}) = \begin{pmatrix} \omega_\lambda \delta_{\lambda\mu} + K_{\lambda\mu}^{++}(\tilde{\omega}) & K_{\lambda\mu}^{+-}(\tilde{\omega}) \\ -K_{\lambda\mu}^{+-*}(-\tilde{\omega}^*) & -\omega_\lambda \delta_{\lambda\mu} - K_{\lambda\mu}^{++*}(-\tilde{\omega}^*) \end{pmatrix} \quad (11)$$

In the Hartree-Fock representation, the elements of the incoherent self-energy are given by,

$$K_{\lambda\mu}^{++}(\tilde{\omega}) = -\frac{1}{4} \sum_{ijkl} \frac{\langle k\ell | [O_\lambda, v] | ij \rangle \langle ij | [O_\mu^\dagger, v] | k\ell \rangle}{\hbar\tilde{\omega} - \Delta\varepsilon_{ijkl}} \mathcal{N}_{ijkl} \quad (12)$$

and

$$K_{\lambda\mu}^{+-}(\tilde{\omega}) = \frac{1}{4} \sum_{ijkl} \frac{\langle k\ell | [O_\lambda, v] | ij \rangle \langle ij | [O_\mu, v] | k\ell \rangle}{\hbar\tilde{\omega} - \Delta\varepsilon_{ijkl}} \mathcal{N}_{ijkl} \quad (13)$$

with  $\mathcal{N}_{ijkl} = (1 - n_i)(1 - n_j)n_k n_\ell - n_i n_j(1 - n_k)(1 - n_\ell)$  and  $\Delta\varepsilon_{ijkl} = \varepsilon_i + \varepsilon_j - \varepsilon_k - \varepsilon_\ell$ , where  $\varepsilon_i$  and  $n_i$  denote energies and Fermi-Dirac occupation numbers of the single-particle states. The collisional self-energy is non diagonal, and therefore it introduces a coupling between different RPA modes through their decay channels, so-called collisional coupling.

In the following, we will neglect the non-diagonal part, which in general introduces a small correction to the strength distributions.

According to [23,24], the expression of the coherent self-energy is given by

$$\begin{aligned} \Sigma_{\mu}^C(\tilde{\omega}) = & \sum_{\lambda ij} \frac{|\langle i|[Q_{\mu}, h_{\lambda}^{\dagger}]|j\rangle|^2}{\hbar\tilde{\omega} - \hbar\omega_{\lambda} - \epsilon_j + \epsilon_i} \mathcal{M}_{\lambda,ij} \\ & - \sum_{\lambda ij} \frac{|\langle i|[Q_{\mu}, h_{\lambda}]|j\rangle|^2}{\hbar\tilde{\omega} + \hbar\omega_{\lambda} - \epsilon_j + \epsilon_i} \mathcal{M}_{\lambda,ji} \end{aligned} \quad (14)$$

where

$$\mathcal{M}_{\lambda,ij} = (N_{\lambda}^0 + 1)(1 - n_j^0)n_i^0 - N_{\lambda}^0 n_j^0(1 - n_i^0) \quad (15)$$

and  $N_{\lambda}^0$  denotes the finite temperature boson occupation factors for the RPA modes  $N_{\lambda}^0 = 1/[\exp(\hbar\omega_{\lambda}/T) - 1]$ . In general, the coherent self-energy is also non-diagonal, and it couples different RPA modes. Here, we neglect this coupling and retain only the diagonal part. The coherent mechanism, which arises from coupling of the single-particle excitations with the mean-field fluctuations in the stochastic transport theory, correspond to the coherent mechanism described in [5,11] and its finite temperature extension using the Matsubara formalism in [14,15].

We can deduce the response function associated with an excitation operator  $A$ , by calculating the expectation value  $\langle A \rangle = \text{Tr} A \delta\rho(t)$  with the help of the expression (8). The corresponding strength distribution is obtained by the imaginary part of the response function and it can be expressed as,

$$S(\tilde{\omega}) = -\frac{1}{\pi} \text{Im} \left( \begin{matrix} A^* & A \end{matrix} \right) (\hbar\tilde{\omega} - \Sigma(\tilde{\omega}))^{-1} \begin{pmatrix} A \\ -A^* \end{pmatrix}. \quad (16)$$

The strength function includes both damping mechanisms, i.e. the collisional damping due to coupling with the incoherent 2p-2h states and the coherent mechanism due to coupling with a low-lying phonon and p-h states.

In our previous studies, we investigated the nuclear collective response in the basis of the incoherent damping mechanism. We found that at low temperature, in particular for

light and medium weight nuclei, the incoherent damping mechanism has a sizeable influence on the strength functions, and it becomes more important at higher temperatures. On the other hand, in particular for heavy nuclei, the coherent mechanism due to coupling of giant resonance with phonons plus p-h states, plays a dominant role for describing the properties of cold giant resonance. In this paper, we want to clarify the relative importance of the incoherent and the coherent mechanisms in collective response in cold nuclei. For this purpose, we present three different calculations by incorporating only the coherent mechanism, only the incoherent mechanism and including both mechanisms in to the calculations, and compare the results with the experimental data.

### III. DETAILS OF THE CALCULATION

#### A. RPA calculation

In order to obtain the solution of equation (10), we first solve the RPA equation (9) in a discrete basis. In order to account partially for the states in the continuum, particle and hole states are obtained by diagonalizing the Hartree-Fock Hamiltonian in a large harmonic oscillator representation [30] which includes respectively 12 major shell for  $^{40}\text{Ca}$  and 15 major shells for other nuclei. We use a fixed imaginary part for the forcing frequency  $\eta = \eta_s = 0.5$  MeV. The Hartree-Fock and RPA calculations are performed using the effective Skyrme force SLy4 [31]. We use the standard excitation operators for isoscalar and isovector resonances for  $L \geq 1$  (for a review see [17]),

$$A_{LM} = \frac{Z}{A} \sum_{i=1}^A r_i^L Y_{LM} \tag{17}$$

$$A_{LM} = \frac{N}{A} \sum_{i=1}^Z r_i^L Y_{LM} - \frac{Z}{A} \sum_{i=1}^N r_i^L Y_{LM}$$

where  $Y_{LM}$  are the spherical harmonics, and for isoscalar giant monopole resonance, we employ

$$A_{00} = \frac{Z}{A} \sum_{i=1}^A r_i^2 Y_{00} \tag{18}$$



The energy-weighted sum rule (EWSR) is given by,

$$m_1 = \sum_{\lambda} \hbar\omega_{\lambda} |\langle 0 | A | \lambda \rangle|^2 \quad (19)$$

When the states  $\lambda$  are specified in the RPA, it can be calculated from the Hartree-Fock ground state according to  $m_1 = \frac{1}{2} \langle [F^{\dagger}, [H, F]] \rangle_0$ . For the Skyrme interactions, it leads to the following expression,

$$\begin{cases} m_1^{GMR} = \frac{2\hbar^2 Z^2}{m A} \langle r^2 \rangle_{HF} \\ m_1^{GDR} = \frac{9}{4\pi} \frac{\hbar^2 NZ}{2m A} (1 - \kappa) \\ m_1^{GQR} = \frac{50}{4\pi} \frac{\hbar^2 Z^2}{2m A} \langle r^2 \rangle_{HF} \end{cases} \quad (20)$$

where  $\langle r^2 \rangle_{HF}$  denotes the root-mean square radius (rms) obtained from the Hartree-Fock ground state. In the case of the Giant Dipole Resonance, the Thomas-Reich Kuhn (TKR) sum rule is violated due to the non-local term in Skyrme forces, and the modification factor is giving by [32,33],

$$\kappa = \frac{2m}{\hbar^2} \left[ t_1 \left( 1 + \frac{1}{2} x_1 \right) + t_2 \left( 1 + \frac{1}{2} x_2 \right) \right] \frac{1}{A} \int \rho_n(r) \rho_p(r) d^3r, \quad (21)$$

where  $\rho_n$  and  $\rho_p$  are the neutron and proton one-body density.

In the following, we compare the result of calculations with the experimental EWSR by employing the standard expression and parameters of the sum-rule [34,35]. In the standard approach, the rms radius is approximated using a Wood-Saxon shape for the one-body density, which leads to the following expression,

$$\langle r^2 \rangle_{WS} = \frac{3}{5} R_0^2 \left( 1 + \frac{7}{3} \left[ \frac{\pi a}{c} \right]^2 \right) \quad (22)$$

where  $R_0$  correspond to the surface position and  $a$  is the diffuseness. Different parameters used in the calculations are reported in table I. In table II, we compare the sum rules obtained by the parameterization (22) and  $\kappa = 0$  and those results obtained from the RPA calculations of (19). The smallness of the difference insures the quality of the RPA calculations.

TABLES

Nucleus	$R_0$	a	$\langle r^2 \rangle_{WS}^{1/2}$	$\langle r^2 \rangle_{HF}^{1/2}$	$\kappa$
	(fm)	(fm)	(fm)	(fm)	
$^{40}\text{Ca}$ [36]	3.65	0.55	3.49	3.40	0.160
$^{90}\text{Zr}$ [35]	4.90	0.515	4.25	4.26	0.177
$^{120}\text{Sn}$ [35]	5.55	0.515	4.71	4.70	0.176
$^{120}\text{Pb}$ [35]	6.67	0.545	5.55	5.55	0.180

TABLE I. Density shape parameters used in the calculations of the sum-rules. Hartree-Fock rms obtained with the Sly4 force are very close to those obtained with the Wood-Saxon parameterization.

Nucleus	$0^+$ (MeV. fm <sup>4</sup> )	$1^-$ (MeV. fm <sup>2</sup> )	$2^+$ (MeV. fm <sup>4</sup> )
$^{40}\text{Ca}$	10103 (9290)	148 (144)	10050 (9226)
$^{90}\text{Zr}$	26664 (26025)	330 (325)	26523 (22556)
$^{120}\text{Sn}$	38295 (37026)	433 (427)	38092 (26477)
$^{208}\text{Pb}$	82633 (84572)	738 (748)	82197 (76034)

TABLE II.  $m_1$  sum rule obtained from standard parameterization of the rms radii. Sum rule calculated from RPA are reported in parenthesis.

## B. Computation of self-energies

### 1. Coherent mechanism.

In order to incorporate the effect of coupling to surface modes, we calculate the RPA response for multipolarities up to  $L = 5$ . The coherent self-energy given by eq. (14) is then calculated by coupling collective states to low-lying states that exhaust at least 1% fraction of the EWSR. Energies and EWSR of collective modes used in the calculation are reported in table III. We note that, in particular, energies of collective  $3^-$  states are overestimated in the RPA calculations. The percentage of the EWSRs are normalized to the RPA sum-rules. In the calculations of the matrix elements in eq.(14), we employ the full SLy4 interaction.

Nucleus	$J^\pi$	E (MeV)	% EWSR
$^{40}\text{Ca}$	$0^+$	17.6	10.4
	$0^+$	19.1	12.5
	$0^+$	20.7	18.1
	$0^+$	22.0	18.0
	$0^+$	24.4	15.5
	$1^-$	16.7	19.5
	$1^-$	17.8	15.0
	$1^-$	18.6	22.8
	$2^+$	17.1	74.9
	$3^-$	5.3	9.5
	$3^-$	7.3	10.8
	$5^-$	5.2	3.7

$^{90}\text{Zr}$	$0^+$	17.8	35.1
	$0^+$	18.6	17.1
	$1^-$	15.7	50.1
	$1^-$	17.9	14.9
	$2^+$	5.4	5.4
	$2^+$	16.3	13.5
	$2^+$	16.4	54.4
	$3^-$	3.7	4.9
	$3^-$	7.9	19.8
	$3^-$	9.4	8.9

---

$^{120}\text{Sn}$	$0^+$	16.8	30.7
	$0^+$	18.4	42.4
	$1^-$	14.1	20.1
	$1^-$	14.5	13.7
	$1^-$	16.9	15.7
	$2^+$	6.0	3.5
	$2^+$	16.5	23.0
	$2^+$	16.6	24.0
	$3^-$	3.8	6.7
	$3^-$	6.9	7.2
	$3^-$	7.6	18.0
	$5^-$	7.0	2.7
	$5^-$	8.3	1.1
	$5^-$	9.5	5.8

---

$^{208}\text{Pb}$	$0^+$	14.4	33.5
	$0^+$	14.7	18.8
	$0^+$	15.0	19.5
	$0^+$	16.4	14.3
	$1^-$	12.8	13.7
	$1^-$	13.2	21.2
	$1^-$	13.7	13.8
	$2^+$	3.7	1.4
	$2^+$	6.1	10.2
	$2^+$	13.0	67.5
	$3^-$	4.9	21.9
	$3^-$	6.7	2.0
	$3^-$	7.2	5.7
	$3^-$	9.1	1.3
	$4^+$	6.6	4.0
	$4^+$	8.9	3.1
	$4^+$	9.3	3.1
	$4^+$	9.6	3.1
	$5^-$	4.8	1.3
	$5^-$	5.7	2.3
	$5^-$	5.9	1.1
	$5^-$	6.7	1.1
	$5^-$	7.7	2.5
	$5^-$	8.2	1.7
	$5^-$	9.3	1.6

$5^-$ 

9.5

1.9

---

---

TABLE III. Collective modes and associated EWSR obtained from RPA that are included in the calculations.

## 2. Incoherent mechanism

We have shown in previous calculation that Skyrme interaction are not adequate to compute the incoherent part of the self-energy due to the presence of high momentum component (also, see [13]). As in previous application [19], we use a modified Skyrme interaction which is obtained by introducing a Gaussian cut-off factor in the matrix elements of the Skyrme force  $v_S$ ,

$$\langle ij|v|kl \rangle = \langle ij|v_S|kl \rangle \cdot \exp\left(-\frac{\beta^2|\langle \mathbf{q}^2 \rangle|}{\hbar^2}\right) \quad (23)$$

in this expression,  $\beta$  describes an effective range of the interaction and the quantity  $\langle \mathbf{q}^2 \rangle$  provides a measure for the relative momentum which is defined by the relation  $\langle ij|\delta(\mathbf{r})|kl \rangle = \langle ij|\mathbf{q}^2\delta(\mathbf{r}) + \delta(\mathbf{r})\mathbf{q}^2|kl \rangle$  with  $\mathbf{r} = \mathbf{r}_1 - \mathbf{r}_2$  and  $\mathbf{q} = (\mathbf{p}_1 - \mathbf{p}_2)/2$ . A quantitative discussion of the influence of  $\beta$  can be found in [22]. In the following, we use  $\beta = 1.4$  fm. The size of the HO basis used to expand the particle and hole (HF) states have been chosen large enough to ensure a convergency of the results with in few per cent.

## IV. RESULTS

We carry out calculations of strength functions for the giant monopole (GMR), the giant dipole (GDR) and the giant quadrupole (GQR) response at zero temperature. The resulting strength distributions are presented for  $^{40}\text{Ca}$  (figure 1),  $^{90}\text{Zr}$  (figure 2),  $^{120}\text{Sn}$  (figure 3) and  $^{208}\text{Pb}$  (figure 4). The left panels of figures show the result of RPA calculations (dashed lines) and the calculations performed by including only the coherent self-energy (thin lines) and only the incoherent self-energy (thick lines). The result of calculations performed by including both self-energies are shown on the right panel of figures (thick lines).

## FIGURES

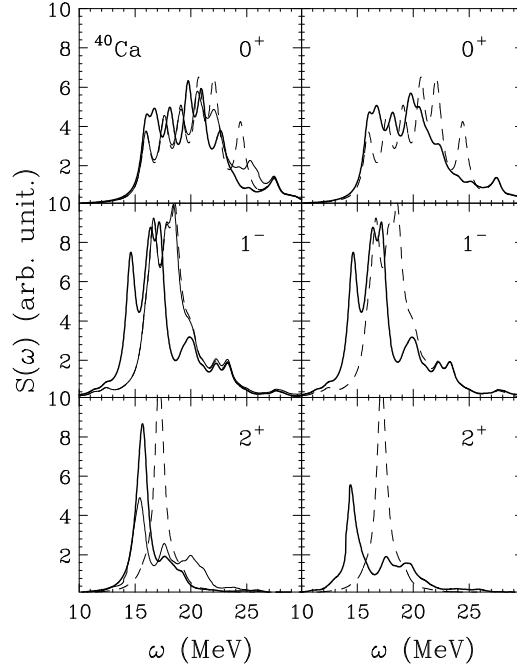


FIG. 1. Calculated strength distributions for GMR (top), GDR (middle) and GQR (bottom) in  $^{40}\text{Ca}$ . Left: strengths obtained in the RPA (dashed lines), with the coherent mechanism (thin lines) and the incoherent mechanism (thick lines). Right: comparison between the RPA (dashed lines) and the extended RPA (thick lines), which includes both the coherent and the incoherent damping mechanisms.



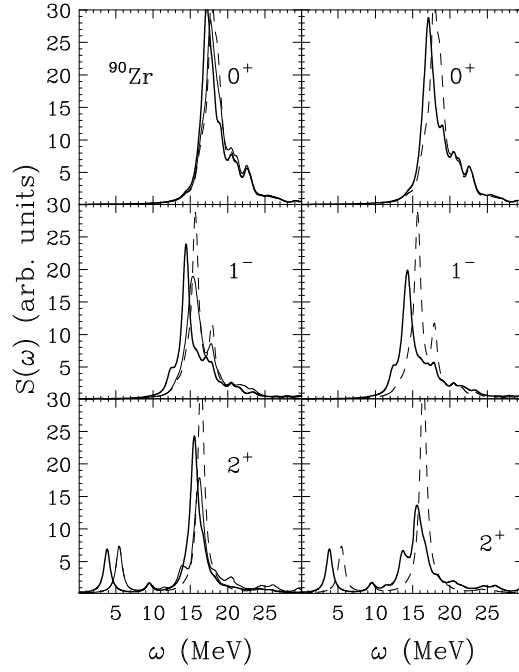


FIG. 2. Same as figure 1 for  $^{90}\text{Zr}$ .

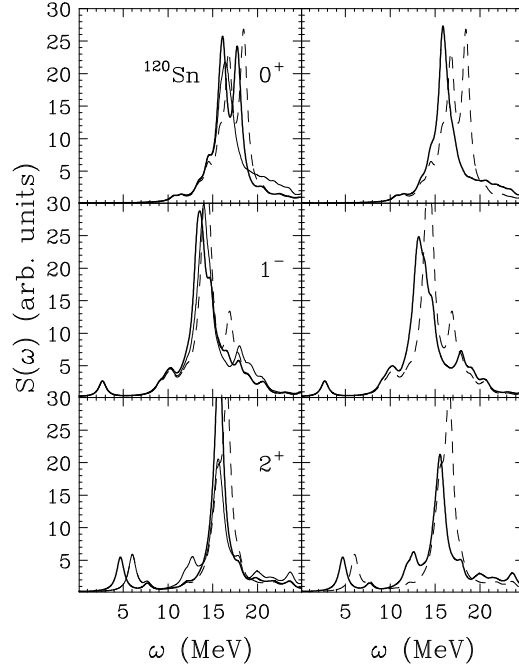


FIG. 3. Same as figure 1 for  $^{120}\text{Sn}$ .

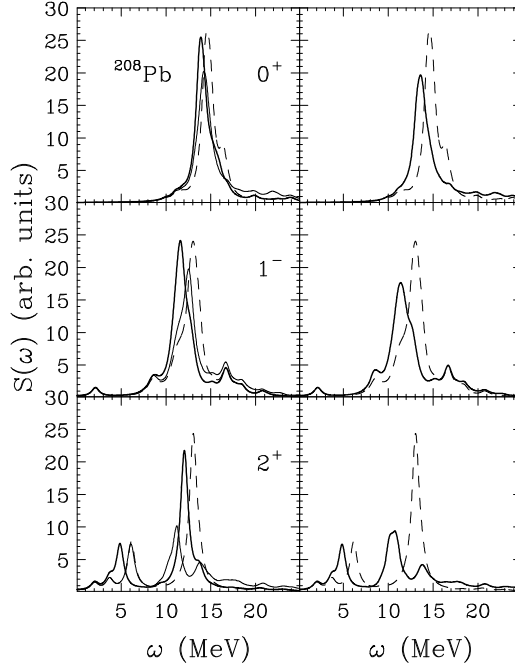


FIG. 4. Same as figure 1 for  $^{208}\text{Pb}$ .

### A. Interplay between incoherent and coherent mechanism

In order to quantitatively discuss the effects of different contributions, it is useful to compute moments of the strength in a given energy interval,

$$m_{i-[E_{min}, E_{max}]} = \int_{E_{min}}^{E_{max}} (\hbar\omega)^i S(\omega) d\omega \quad (24)$$

From these moments, we can define various mean energies  $\overline{E}_i = m_i/m_{i-2}$ . An estimation of the spreading of the strength is given by the width  $\overline{\Gamma} = \sqrt{m_2/m_0 - (m_1/m_0)^2}$ . In figure 5, the difference  $\Delta E = \overline{E}_1 - \overline{E}_1^{RPA}$  between the mean energy obtained in different calculations and the mean-energy calculated in the RPA is plotted as a function of the mass number for the different multipolarities. In figure, calculations by including the coherent mechanism, the incoherent mechanism and the coherent plus incoherent are indicated by dashed lines, dashed-dotted lines and solid lines, respectively. In figure 6, a similar plot is presented for the deviation of the width from the RPA response,  $\Delta\Gamma = \overline{\Gamma} - \overline{\Gamma}^{RPA}$ . In these calculations,

moments of the strength functions are evaluated over the energy interval 0-40 MeV. From the results of calculations, we can draw the following conclusions:

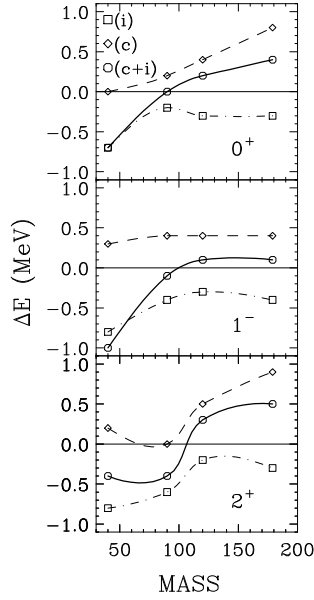


FIG. 5. Variation of the mean-energy  $\Delta\bar{E} = \bar{E}_1 - \bar{E}_1^{RPA}$  calculated in the energy interval 0-40 MeV for GMR (top), GDR (middle) and GQR (bottom) as a function of mass number. Calculations performed by including the coherent mechanism, the incoherent mechanism and both coherent and incoherent mechanisms are indicated by dashed lines, dash-dotted lines and solid lines, respectively.

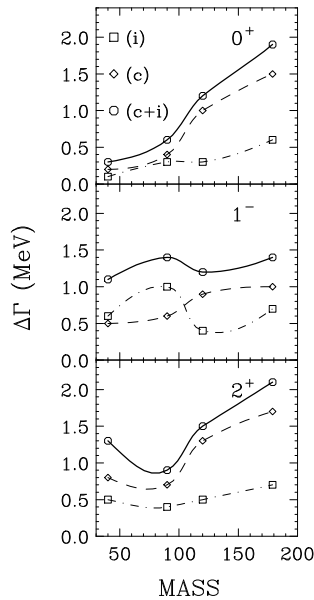


FIG. 6. Variation of the mean-width  $\Delta\bar{E} = \bar{E}_1 - \bar{E}_1^{RPA}$  calculated in the energy interval 0-40 MeV for GMR (top), GDR (middle) and GQR (bottom) as a function of mass number. Calculations performed by including the coherent mechanism, the incoherent mechanism and both coherent and incoherent mechanisms are indicated by dashed lines, dash-dotted lines and solid lines, respectively.

- **Shift of mean-energy:**

- The incoherent mechanism induces a reduction of the mean energy, while the coherent part acts in the opposite way. The origin of this phenomenon can be found by looking carefully in figures from 1 to 4. Indeed, we note that both coherent and incoherent self-energies induces a shift of the main peaks towards lower energy. However, at the same time, a part of strength is shifted toward higher energy in the coherent case, which gives rise to a global increase of the average mean-energy. Such a behavior can be understood by looking at self-energies themselves. An example, in figure 7, the coherent (thin lines) and the incoherent (thick lines) self-energies are shown for the GQR in  $^{40}\text{Ca}$ . We see that the energy dependence of the real part of the self-energy is different in two different mechanisms. While the incoherent mechanism induces a global shift of the strength towards lower energies, the real part of the coherent self-energy change of sign in the vicinity of the collective energy. This introduces a shift toward lower energy of the low energy part of the strength while the high energy part is pushed towards higher energies. In some cases, we may even expect that a single resonance is splitted into two peaks, as it happens for the GQR in  $^{40}\text{Ca}$ .
- For the GQR and GMR in lighter nuclei, the shift introduced by the incoherent mechanism is stronger than the coherent one. On contrary, the tendency goes the opposite direction for heavier nuclei. For the GDR, both effects are comparable.
- In all cases, the effect of the incoherent mechanism is of the same order of magnitude as that of the coherent mechanism and can not be neglected in contrast to the usual assumption [18].

- **Increase of spreading width:**

- Both the coherent and incoherent self-energy induces an increase of the spreading.
- In the case of the GQR and GMR, the coherent damping is always much larger than the incoherent one while for the GDR both are of same order. For instance, in the GQR case, where the strength is in general not Landau fragmented, we can see that the coupling to surface modes induces a splitting of the main pic of the RPA into different peaks. In the calcium case, this effect can be related to the presence of two collective low-lying  $3^-$  states strongly coupled to the GQR.
- The fact that the coherent mechanism induces a larger damping can be seen by looking at bottom panel of figure 7. In this particular example, we see that the imaginary part of the self-energy is larger for the coherent mechanism than for the incoherent case, which gives a larger damping width.
- When the strength is already largely Landau fragmented (like in the GMR of  $^{40}\text{Ca}$ ) both incoherent and coherent effects seems almost negligible.
- The magnitude of the coherent mechanism becomes larger for heavier nuclei.

- **Additivity of coherent and incoherent effects:**

- The shift in the mean energy,  $\Delta E$ , and the increase of the width,  $\Delta\Gamma$ , are approximately given by the sum of these quantities obtained by considering the coherent and incoherent mechanisms separately.

The effects of both, coherent as well as incoherent mechanisms appears to be more significant for the lighther nuclei as seen from figures 1-4. This may be due to the fact that in lighther nuclei a large fraction of nucleons resides in the vicinity of nuclear surface relative to the heavier ones, where the predominant effects of both coherent as well as incoherent mechanisms occur. Moreover, in light nuclei the energy of the collective states is higher leading to an increase of the damping width.

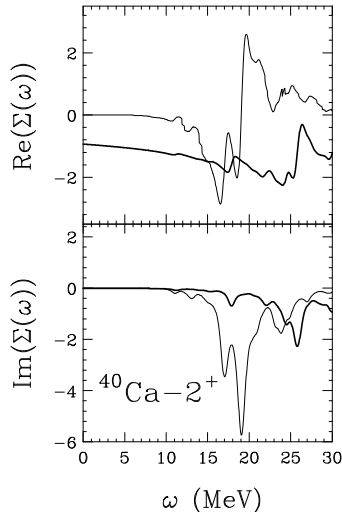


FIG. 7. The real (top) and the imaginary (bottom) part of the coherent (thin line) and the incoherent (thick line) part of the self-energies for the GQR in  $^{40}\text{Ca}$ .

### B. Fragmentation of response

With the high precision experiments, it is possible to determine fragmentation and fine structure of the strength functions. In order to characterize systematically the shape of strength functions, we present properties of giant resonances spectra in tables IV - XV. Depending on the fragmentation of each response, we report average mean energies and width for different energy intervals. When the strength is divided into several main peaks, we consider energy intervals around the main peaks. Besides the average properties, we also report the main peak positions. We emphasize that, in particular for the GQR response, the coherent mechanism induces an additional fragmentation of the strength. The incoherent mechanism also introduces such a fragmentation, but it is much weaker than the coherent effect. The incoherent damping strongly the peak positions. In any case, for a proper description of the fragmentation and the fine structure of the strength distributions, both the coherent and the incoherent mechanisms should be taken into the description.

### C. Low-lying states

The RPA calculations, most often, overestimate the mean-energy of low-lying states. We find that the incoherent mechanism reduces systematically the mean-energy of the GQR states for medium and heavy nuclei. In table IX, XII and XV, we can see that the mean-energy of the low-lying  $2^+$  states is shifted by -1.3 MeV for  $^{90}\text{Zr}$  and  $^{120}\text{Sn}$ , and by -0.7 MeV in  $^{208}\text{Pb}$ . Such a shift is absent in the calculations with the coherent damping mechanism, while it remains when the both mechanisms are included into the description.

### D. Comparison with experiment

When the strength is highly fragmented, a direct comparison to experimental data is hardly possible. Experiments are often analyzed using a fitting plus folding procedure of spectra which mix different multiplicities [34]. From this procedure, one extract energy ( $E_\alpha$ ), width ( $\Gamma_\alpha$ ) and percentage of the EWSR ( $(\%EWSR)_\alpha$ ). In order to compare with experimental data, we convert the experimental data into percentages of the EWSR in given energy intervals, which is determined according to

$$\begin{aligned}
 (\%EWSR)_{[E_{min}, E_{max}]} &= \sum_{\alpha} (\%EWSR)_{\alpha} \\
 &\times \int_{E_{min}}^{E_{max}} \frac{\Gamma_{\alpha}/2\pi}{(E-E_{\alpha})^2 - \Gamma_{\alpha}^2/4}
 \end{aligned}
 \tag{25}$$

In this expression,  $\alpha$  runs over different states of considered multiplicity, and a Lorentzian shape is assumed for each mode in the calculations. We note that Gaussian shapes rather than Lorentzian only slightly change the reported values. In tables IV - XV, we compare the results of our calculations for the percentage of EWSR with experiments in the energy interval around the peak energy of the corresponding giant resonance. In all cases, our calculations provide a good description for the experiments. In general, the introduction of coherent and incoherent mechanisms gives a better description of available experimental data. However, in some cases, the percentage of the EWSR obtained in RPA already gives

the good order of magnitude. We pay particular attention to the GQR excitations in  $^{40}\text{Ca}$  and  $^{208}\text{Pb}$ , since both have been extensively studied experimentally and have given long-standing discussions [1].

*1. Splitting of the  $2^+$  resonance in  $^{40}\text{Ca}$*

The GQR response in  $^{40}\text{Ca}$  is known to be split into two components with energy around 13.5 and 18 MeV with almost an equal fraction of the EWSR (around 30 % to 40 % for both peaks). The description of this fragmentation by microscopic calculations is a problem. Only recently [16,17], microscopic calculations assuming ground state correlations and coupling to low lying states reproduce a global splitting. However, these calculations describe the global trend of the response and do not provide an explanation for the equal partition of the strength.

Looking at table VI, we see that, our calculation with the coherent and incoherent mechanism not only reproduce splitting of the strength into two main components (see figure 1) but also give rise to an equal splitting around the main peak (31 % in the interval 10-16 MeV and 33.6 % in the interval 16-22 MeV), that matches with the experimental data. When only the coherent self-energy is included, the calculations can not reproduce the splitting, but give the percentage of the EWSR, which are comparable to those obtained in ref. [17] i.e. a too high percentage of the EWSR for the second peak and a too low for the first one.

This particular example demonstrates the necessity of taking both coherent and incoherent damping mechanisms at the same time and illustrates the complementarity of the two effects. Indeed, without the coherent mechanism splitting of the strength is not found while without the incoherent damping the EWSR is not reproduced.



## 2. Fine structure in $^{208}\text{Pb}$

The calculated strength obtained in our microscopic calculations for the GQR of  $^{208}\text{Pb}$  is displayed in bottom panel of figure 4. As in the case of  $^{40}\text{Ca}$ , global shape of the strength exhibits a splitting of the GQR response into two main peaks at 10.8 MeV and 13.8 MeV. The first peak is well known and is correctly reproduced by our calculations, while the RPA alone does not give a correct description. However the fraction of the EWSR is slightly smaller as compared to the experiment (see bottom of table XV). The second peak has never been observed but is also present in second RPA calculations [4,7].

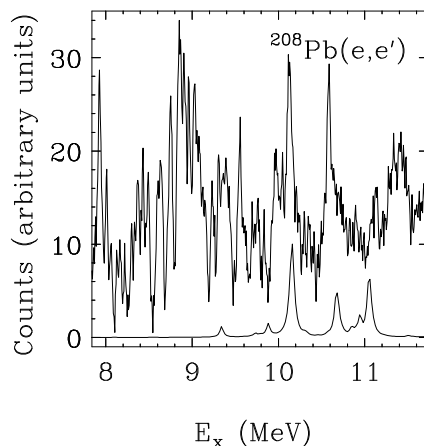


FIG. 8. Thin line: the strength function for GQR in  $^{208}\text{Pb}$ , which is calculated including the coherent and the incoherent self-energies with a smoothing parameter  $\eta = \eta_s = 0.025$  MeV. Thick line: the experimental spectra obtained in the inelastic electron scattering experiment.

Our calculation, which assume a rather large value of the smoothing parameter only gives a global shape of the strength distributions. In order to reveal the fine structure on top of the global shape, we also perform calculation s with smaller smoothing parameter  $\eta = \eta_s = 0.025$  MeV which corresponds to experimental resolution. The corresponding strength distribution is presented in figure 8 for the collective energy region 7.6 - 11.8 MeV. The calculated response is compared with the inelastic electron scattering data [2]. This experimental data presents a well-defined fine structure which is also observed with a one-to-one correspondence in  $(p,p')$  experiments [70,3]. In figure 8, we see that the calculations

agree with the part of spectral properties of the peaks in the vicinity of the collective energy. However, we note that below 9 MeV, the fine structure is almost absent in our description. The peak positions observed experimentally and obtained in our calculations are reported in table XVI. We can see from this table that fine structures are already present in the coherent case while they are absent in the incoherent one. When both effects are included, it seems that part of the peaks are perfectly located as compared to recent (p,p') experiments. It has been recently discussed that other peaks might be coming from dipole excitations [71]. It is also possible that missing peaks might be due to the fact that part of the two-body correlations are neglected in the present description or coming from higher order correlations.

## V. CONCLUSION

In this article, we carry out a systematic investigation the effect of coherent and incoherent damping mechanisms on the collective response in spherical nuclei at zero temperature. Our calculations indicate that both mechanisms play important roles in a proper description of the nuclear collective response. An extensive comparison with experimental data is presented in terms of the fraction of exhausted EWSR for the GMR, GQR and GDR for a number of nuclei. We show that the presented calculations are in reasonable agreement with the observed collective response. A special attention has been given to the GQR response in calcium and lead nuclei where a large amount of experimental and theoretical work exists. In particular, we show that, while the usual mean-field theory is unable to explain the equal splitting of the  $2^+$  state, the inclusion of both coherent and incoherent damping mechanism provides an explanation for fragmentation of the GQR response. Furthermore, by reducing smoothing parameter in the calculations, we observe the appearance of fine structure on top of the global fragmentation in the strength functions. A comparison with high resolution experiment shows that part of the observed peaks energies are located very close to the calculated energies.

Our study demonstrates the importance of coupling to low-lying surface modes for the

understanding of fine structures in collective response. For this purpose, the extended mean-field description that includes both the incoherent and the coherent mechanisms in an consistent manner appears as a promising tool for the understanding of fine-structure properties in the fragmentation of giant resonance excitations. It will be interesting to carry our similar investigations at finite temperature.

### **Acknowledgments**

We thank A. Richter for providing the  $(e,e')$  data. One of us (S. A.) gratefully acknowledges GANIL Laboratory for a partial support and warm hospitality extended to him during his visits to Caen. This work is supported in part by the US DOE grant No. DE-FG05-89ER40530.

## REFERENCES

- [1] A. van der Woude, *Electric and Magnetic Giant Resonances in Nuclei* (World Scientific, 1991) p. 101 (and reference therein), edited by J. Speth.
- [2] G. Kühner, D. Meuer, S. Müller, A. Richter, E. Spamer, O. Titze and W. Knüpfner, *Phys. Lett.* **104B** (1981) 189.
- [3] S. Kamerdzhiev, J. Lisantti, P. von Neumann-Cosel, A. Richter, G. Tertychny and J. Wambach, *Phys. Rev.* **C55** (1997) 2101.
- [4] D. Lacroix, A. Mai, P. von Neumann-Cosel, A. Richter and J. Wambach, *Phys. Lett.* **B479** (2000) 15.
- [5] G. F. Bertsch, P.F. Bortignon and R. A. Broglia, *Rev. Mod. Phys.* **55** (1983) 287.
- [6] G.F. Bertsch and R.A. Broglia, *Oscillation in finite quantum systems*, Cambridge (1994).
- [7] S. Drozdz, S. Nishizaki, J. Speth and J. Wambach, *Phys. Rep.* **197** (1990) 1.
- [8] D. Lacroix and Ph. Chomaz, *Phys. Rev.* **C60** (1999) 064307.
- [9] K.Goeke and P.-G.Reinhard, *"Time-Dependent Hartree-Fock and Beyond"*, Proceedings, Bad Honnef, Germany (1982).
- [10] Y. Abe, S. Ayik, P. G. Reinhard and E. Suraud, *Phys. Rep.* **275** (1996) 49.
- [11] P.F. Bortignon and R. Broglia, *Nucl. Phys.* **A371** (1981) 405.
- [12] S. Ayik, O. Yilmaz, A. Gokalp and P. Schuck, *Phys. Rev.* **C58** (1998), 1594.
- [13] O. Yilmaz, A. Gokalp, S. Yildirim and S. Ayik, *Phys. Lett.* **B472** (2000) 258.
- [14] P. Bortignon, R. A. Broglia, G. F. Bertsch and J. Pacheco, *Nucl. Phys.* **A460** (1986) 149.
- [15] N. Giovanardi, P.F. Bortignon and R.A. Broglia, *Nucl. Phys.* **A641** (1998) 95.

- [16] S. Kamezdzhiev, J. Speth and G. Tertychny, Phys. Rev. Lett. **72** (1995) 1995.
- [17] S. Kamezdzhiev, J. Speth and G. Tertychny, Nucl. Phys. **A624** (1997) 328.
- [18] F.V. De Blasio, W. Cassing, M. Tohyama, P.F. Bortignon, and R. Broglia, Phys. Rev. Lett. **68** (1992) 1663.
- [19] D. Lacroix, Ph. Chomaz and S. Ayik, Phys. Rev. **C 58** (1998) 2154.
- [20] S. Ayik, D. Lacroix and Ph. Chomaz, Phys. Rev. **C 61** (2000) 014608.
- [21] Ph. Chomaz, D. Lacroix, S. Ayik and M. Colonna, Phys. Rev. **C62** (2000) 024307.
- [22] D. Lacroix, Ph. Chomaz and S. Ayik, Phys. Lett. **B489** (2000) 137.
- [23] S. Ayik, preprint YITP-00-23 and Phys. Lett. **B** (2000) *in press*.
- [24] S. Ayik and Y. Abe, preprint YITP-00-55 and submitted to Phys. Rev. **C** (2000).
- [25] S. Ayik, Z. Phys. **A350** (1994) 45.
- [26] Y. B. Ivanov and S. Ayik, Nucl. Phys. **A593** (1995) 233.
- [27] A. Guarnera, M. Colonna and P. Chomaz, Phys. Lett **B373**, (1996) **267**.
- [28] J. D. Frankland *et al*, Preprint nucl-ex/0007019, Preprint nucl-ex/0007020.
- [29] P. Ring and P. Schuck, *The nuclear many-body problem*, *Spring-Verlag*, New-York (1980).
- [30] N. Van Giai and H. Sagawa, Nucl. Phys. **A371** (1981) 1.
- [31] E. Chabanat, P. Bonche, P. Haensel, J. Meyer and R. Schaeffer, Nucl. Phys. **A627** (1997) 710; Nucl. Phys. **A635** (1997) 231. Erratum: Nucl. Phys. **A643** (1998) 441.
- [32] H. Sagawa and G.F. Bertsch, Phys. Lett. **B146** (1984) 138.
- [33] M. Barranco, A. Polls, S. Marcos, J. Navarro and J. Treiner, Phys. Lett. **B154** (1985) 96.

- [34] G.R. Satchler, Nucl. Phys. **A472** (1987) 215.
- [35] D.J. Horen, J. R. Beene and G. R. Satchler, Phys. Rev. **C52** (1995) 1554 (and reference therein).
- [36] D. H. YoungBlood, Y.-W. Lui and H. L. Clark, Phys. Rev. **C55** (1997) 2811.
- [37] S. Brandenburg *et al*, Phys. Lett. **B130** (1983) 9. S. Brandenburg *et al*, Nucl. Phys. **A466** (1987) 29.
- [38] M Kohl, P. von Neumann-Cosel, A. Richter, G. Schrieder and S. Strauch, Phys. Rev. **C57** (1998) 3167.
- [39] J. Hahrens *et al* , Proc. of the Int. Conf. on nuclear structure, Sendai, Japan, 1972.
- [40] H. Diesener *et al*, Phys. Rev. Lett. **72** (1994) 1994.
- [41] J. Ahrens *et al*, Nucl. Phys. **A251** (1975) 479.
- [42] S. Kamerdzhiev, J. Speth, G. Tertychny and V. Tselyaev, Nucl. Phys. **A555** (1993) 90. (Table 1).
- [43] F. Zwarst, A.G. Drentje, M.N. Harakeh and A. Van der Woude, Nucl. Phys. **A439** 117.
- [44] T. Yamagata *et al*, Phys. Rev. **C36** (1987) 573.
- [45] J. Lisantti *et al*, Phys. Rev. **C40** (1989) 211.
- [46] H. Diesener *et al*, Phys. Lett. **B352** (1995) 201.
- [47] F.E. Bertrand, G.R. Satchler, D.J. Horen and A. van der Woude, Phys. Lett. **B198** (1979) 198.
- [48] S. Shlomo and D.H. Youngblood, Phys. Rev. **C47** (1993) 529 (and reference therein).
- [49] D.H. Youngblood, P. Kogucki, J.D. Bronson, U. Garg, Y.-W. Lui and C. M. Rozsa, Phys. Rev. **C23** (1981) 1997.

- [50] R. Liguori Neto *et al*, Nucl Phys. **A560** (1993) 733.
- [51] T. Suomijarvi *et al*, Nucl Phys. **A491** (1989) 314.
- [52] T. Suomijarvi *et al*, Nucl Phys. **A509** (1990) 369.
- [53] B.L. Berman and S. C. Fultz, Rev. Mod. Phys. **47** (1975) 713.
- [54] B. L. Berman, J. T. Cadwell, R. R. Harvey, M.A. Kelly, R. L. Bramblett and S. C. Fultz, Phys. Rev. **162** (1967) 1098.
- [55] A. Leprêtre, H. Beil, R. Bergère, P. Carlos, A. Veyssière and M. Sugarawa, Nucl. Phys **A175** (1971) 609.
- [56] F.E. Bertrand et al, Phys. Rev. **C22** (1980) 1832.
- [57] G. Duhamel, M. Buenerd, P. de Saintignon, J. Chauvin, D. Lebrun, Ph. Martin and G. Perrin, Phys. Rev. **C38** (1988) 2509.
- [58] M. M. Sharma, W. T. A. Borghols, S. Brandenburg, S. Crona, A. Van der Woude and M. H. Harakeh, Phys. Rev. **C38** (1988) 2562.
- [59] S. C. Fultz, B. L. Berman, J. T. Caldwell, R. L. Bramlett and M. A. Kelly, Phys. Rev. **186** (1969) 1255.
- [60] H. P. Morsch, C. ükösd, M. Rogge, P. Turek, H. Machner and C. Mayer-Böricke, Phys. Rev. **C22** (1980) 489. H. P. Morsch, M. Rogge, P. Turek, C. Mayer-Böricke and P. Decowski Phys. Rev. **C25** (1982) 939.
- [61] F.E. Bertrand, *et al*, Phys. Rev. **C34** (1986) 45.
- [62] M. Buenerd, D. Lebrun, Ph. Martin, P. de Saintignon and G. Perrin, Phys. Rev. Lett. **45** (1980) 1670.
- [63] J.R. Beene *et al*, Phys. Rev. **C41** (1990) 920.
- [64] R. R. Harvey, J. T. Caldwell, R. L. Bramlett and S. C. Fultz, Phys. Rev. **136** (1964)

B126.

- [65] A. Veyssière, H. Beil, R. Bergère, P. Carlos, A. Leprêtre, Nucl. Phys. **A159** (1970) 561.
- [66] L. M. Young, PhD Thesis (1972), University of Illinois (unpublished).
- [67] B.L. Berman and S. C. Fultz, Rev. Mod. Phys. **47** (1975) 713.
- [68] D.K McDaniels *et al*, Phys. Rev. **C33** (1986) 1943.
- [69] G.S. Adams *et al*, Phys. Rev. **C33** (1986) 2054.
- [70] J. Lisantti, E. J. Stephenson, A. D. Bacher, P. Li, R. Sawafta, P. Schwandt, S. P. Wells, S. W. Wissink, W. Unkelbach, and J. Wambach, Phys. Rev. C **44**, R1233 (1991).
- [71] A. Drouart, PhD Thesis SPhN-Saclay, France, *to be published*.

$^{40}\text{Ca} / 0^+$	RPA	(c)	(i)	Theory (c+i)	Experiment
$\overline{E}_1$ -[0-40]	21.1	21.1	20.4	20.4	
$\overline{E}_3$ -[0-40]	22.6	22.7	22.0	22.2	
$\overline{\Gamma}$ -[0-40]	4.6(4.0)	4.8(4.2)	4.7(4.1)	4.9(4.4)	
$\overline{E}_1$ -[8-29]	20.6	20.5	19.8	19.8	18.9(0.1) ( $\alpha, \alpha'$ ) [36]
$\overline{E}_3$ -[8-29]	21.4	21.4	20.7	20.7	21.3(0.12) ( $\alpha, \alpha'$ ) [36]
$\overline{\Gamma}$ -[8-29]	3.4(3.1)	3.5(3.2)	3.4(3.1)	3.5(3.2)	4.70(0.11) ( $\alpha, \alpha'$ ) [36]
% EWSR	%	%	%	%	%
[0 – 40]	87.9	88.4	84.1	83.6	
[12.5 – 22.5]	54.2	54.4	63.8	56.8	50 ( $\alpha, \alpha'$ ) [36]
[22.5 – 28.5]	25.6	25.6	18.8	18.6	34.7 ( $\alpha, \alpha'$ ) [36]
[7.5 – 28.8]	80.6	80.9	77.1	76.2	92 ( $\alpha, \alpha'$ ) [36]
[11 – 19]	21.6	22.1	26.9	27.8	44.2 $\pm$ 8.8 (e,e' $\alpha$ ) [38]
[10.5 – 20]	29.1	30.0	36.4	37.0	30 $\pm$ 6 ( $\alpha, \alpha'$ ) [37]



TABLE IV. Properties of GMR in  $^{40}\text{Ca}$ . Top: calculated mean-energy  $\overline{E}_1$  and  $\overline{E}_3$  and width  $\overline{\Gamma}$  obtained by integrating moments of the strength in different energy intervals. Calculations are carried out within RPA, and by including the coherent, the incoherent and the coherent plus incoherent damping mechanisms, which are indicated in columns under (c), (i) and (c+i), respectively. When available experimental data are also reported in the right column. We also display the calculated width for  $\eta_s = 100\text{keV}$  in parenthesis. Bottom: percentage of the EWSR calculated in different energy intervals. In the right column, if available, the corresponding experimental sum rules are also reported together with the reactions and references.

$^{40}\text{Ca} / 1^-$	RPA	(c)	(i)	Theory (c+i)	Experiment
$\overline{E}_1$ -[0-40]	18.8	19.1	18.0	17.8	
$\overline{E}_3$ -[0-40]	20.3	21.1	20.3	20.9	
$\overline{\Gamma}$ -[0-40]	4.4(3.7)	4.9(4.4)	5.0(4.6)	5.5(5.0)	
$E_{peak}$	16.7	16.7	14.6	14.6	
	18.6	18.4	16.4	17.2	$\overline{E} = 19.0$ [39] $\Gamma = 4.0$ [39]
% EWSR	%	%	%	%	%
[0 – 40]	99.3	98.3	88.9	91.5	
[10 – 21.5]	71.0	71.2	65.7	65.1	58(15) (e,e') [40] 63.0 ( $\gamma, x$ ) [41,42]
[21.5 – 40]	27.9	26.8	22.6	25.9	30.6 ( $\gamma, x$ ) [41,42]

TABLE V. Same as table IV for the GDR in  $^{40}\text{Ca}$ . In addition, in middle panel,  $E_{peak}$  indicates the positions of the main peaks of the calculated strengths, and the experimental peak position and the width of giant resonances are denoted by  $\overline{E}$  and  $\Gamma$ .

$^{40}\text{Ca} / 2^+$	RPA	(c)	(i)	Theory (c+i)	Experiment
$\overline{E}_1\text{-}[0-40]$	17.7	17.9	16.9	17.3	
$\overline{E}_3\text{-}[0-40]$	18.8	19.6	18.5	19.4	
$\overline{\Gamma}\text{-}[0-40]$	3.5(2.6)	4.3(3.6)	4.0(3.4)	4.8(4.2)	
$\overline{E}_1\text{-}[10-16]$	14.6	14.8	15.0	14.3	
$\overline{E}_3\text{-}[10-16]$	14.8	14.9	15.1	14.4	
$\overline{E}_1\text{-}[16-22]$	17.6	18.7	17.7	18.6	
$\overline{E}_3\text{-}[16-22]$	17.7	18.9	17.8	18.8	
$E_{peak}$	17.2	15.4	15.7	14.4	13.5 [43,40]
		17.6		17.6	18.0 [43,40]
		20.0		19.3	
% EWSR	%	%	%	%	%
[0 – 40]	92.4	86.6	84.7	87.6	
[13.2 – 15.2]	23.4	12.7	10.7	11.1	$7.6 \pm 1.1$ (p,p') [44]
[13.2 – 16]	29.1	16.3	13.3	14.3	$24.9 \pm 5$ (p,p') [45]
[10 – 16]	0.0	26.6	39.1	31.0	$33 \pm 7$ (e, e'x) [40,46] 60(15) ( $\alpha, \alpha' \alpha_0$ ) [43] (compilation from [46])
[16 – 22]	72.5	51.6	34.7	33.6	$28.6 \pm 7$ (p,p') [47] ( $\alpha, \alpha' \alpha_0$ ) $\sim 40$ [43] 44 (p,p') [45]

TABLE VI. Same as table IV for the GQR in  $^{40}\text{Ca}$ .

$^{90}\text{Zr} / 0^+$	RPA	(c)	(i)	Theory (c+i)	Experiment
$\overline{E}_{1-[0-40]}$	19.0	19.2	18.8	19.0	
$\overline{E}_{3-[0-40]}$	20.0	20.5	20.0	20.4	
$\overline{\Gamma}_{-[0-40]}$	3.6(2.8)	4.0(3.3)	3.9(3.1)	4.2(3.5)	
$E_{peak}$	17.9	17.7	17.2	17.1	$\overline{E} \simeq 16.0$ [48] $\Gamma \simeq 3.3$ [48]
% EWSR	%	%	%	%	%
[0 – 40]	96.6	98.6	93.1	95.6	
[12 – 20]	66.3	70.5	69.3	65.3	$44 \pm 20$ (p,p') [47] $64 \pm 14$ ( $\alpha, \alpha'$ ) [49] $86 \pm 15$ ( $^{17}\text{O}+^{90}\text{Zr}$ ) [50] $83 \pm 14$ ( $^{20}\text{Ne}+^{90}\text{Zr}$ ) [51] $55 \pm 13$ ( $^{40}\text{Ar}+^{90}\text{Zr}$ ) [52]

TABLE VII. Same as table IV for the GMR in  $^{90}\text{Zr}$ .

$^{90}\text{Zr} / 1^-$	RPA	(c)	(i)	Theory (c+i)	Experiment
$\overline{E}_{1-[0-40]}$	16.8	17.2	16.4	16.7	
$\overline{E}_{3-[0-40]}$	18.2	19.0	18.7	19.3	
$\overline{\Gamma}_{-[0-40]}$	3.8(3.0)	4.4(3.8)	4.8(4.2)	5.2(4.7)	
$E_{peak}$	15.7	15.3	14.4	14.3	
	17.9	17.8			$\overline{E} = 16.85$ [67]
					$\Gamma = 4.0$ [67]
% EWSR	%	%	%	%	%
[0 – 40]	96.6	99.7	90.9	93.1	
[11 – 19]	74.5	69.7	66.7	63.7	57 ( $\gamma, x$ ) [54]
					68 ( $\gamma, x$ ) [55]
					$53 \pm 13$ ( $\alpha, \alpha'$ ) [56]
					$63 \pm 14$ ( $^{20}\text{Ne} + ^{90}\text{Zr}$ ) [51]
					$70 \pm 28$ ( $^{40}\text{Ar} + ^{90}\text{Zr}$ ) [52]

TABLE VIII. Same as table IV for the GDR in  $^{90}\text{Zr}$ .

$^{90}\text{Zr} / 2^+$	RPA	(c)	(i)	Theory (c+i)	Experiment
$\overline{E}_1\text{-}[11-25]$	16.8	16.8	16.2	16.4	
$\overline{E}_3\text{-}[11-25]$	17.0	17.5	16.7	17.2	
$\overline{\Gamma}\text{-}[11-25]$	1.9(1.4)	2.6(2.4)	2.3(1.9)	2.8(2.6)	
$\overline{E}_1\text{-}[0-8]$	5.2	5.2	3.9	3.9	
$\overline{E}_3\text{-}[0-8]$	5.6	5.4	4.5	4.6	
$\overline{\Gamma}\text{-}[0-8]$	1.3(0.6)	1.3(0.6)	1.3(0.7)	1.3(0.7)	
$E_{peak}$	5.6	5.6	3.8	3.8	
	9.5	9.5	9.5	9.5	
		13.9		13.7	
	16.4	16.2	15.5	15.6	$\overline{E} = 14.1(0.5)$ [56]
					$\Gamma = 4.0(0.5)$ [56]
% EWSR	%	%	%	%	%
[0 – 40]	84.3	85.1	80.2	80.9	
[11 – 25]	71.7	63.3	71.6	59.1	
[0 – 8]	4.6	4.6	3.1	3.1	
[10 – 18]	57.5	44.7	53.7	43.6	$42 \pm 10$ (p,p') [47]
					$46 \pm 9$ ( $\alpha, \alpha'$ ) [56]
					$46 \pm 14$ ( $^{20}\text{Ne}+^{90}\text{Zr}$ ) [51]
					$23 \pm 14$ ( $^{40}\text{Ar}+^{90}\text{Zr}$ ) [52]

TABLE IX. Same as table IV for the GQR in  $^{90}\text{Zr}$ .

$^{120}\text{Sn} / 0^+$	RPA	(c)	(i)	Theory (c+i)	Experiment
$\overline{E}_1\text{-}[0-40]$	17.4	17.8	17.1	17.6	
$\overline{E}_3\text{-}[0-40]$	18.6	19.7	18.6	19.7	
$\overline{\Gamma}\text{-}[0-40]$	3.6(2.7)	4.6(4.0)	3.9(3.1)	4.8(4.2)	
$E_{peak}$	16.8	16.4	16.1	15.9	
	18.5		17.7		$\overline{E} \simeq 15.3$ [48]
					$\Gamma \simeq 3.7$ [48]
% EWSR	%	%	%	%	%
[0 – 40]	95.9	94.7	93.8	91.7	
[8 – 20]	90.2	65.5	77.1	65.0	
[12 – 20]	78.7	63.6	75.0	63.0	61 ± 15 (p,p') [47]
					72 ± 14 ( $\alpha, \alpha'$ ) [56]
					120 ( $\alpha, \alpha'$ ) [49]
					74 ± 15 ( $\alpha, \alpha'$ ) [57]
					64.6 ± 14 ( $\alpha, \alpha'$ ) [58]
					94. ± 20 ( $^{17}\text{O}+^{120}\text{Sn}$ ) [50]

TABLE X. Same as table IV for the GMR in  $^{120}\text{Sn}$ .

$^{120}\text{Sn} / 1^-$	RPA	(c)	(i)	Theory (c+i)	Experiment
$\overline{E}_1\text{-}[0-40]$	14.8	15.2	14.5	14.9	
$\overline{E}_3\text{-}[0-40]$	16.6	18.0	17.0	18.2	
$\overline{\Gamma}\text{-}[0-40]$	4.4(3.7)	5.3(4.8)	4.8(4.3)	5.6(5.1)	
$\overline{E}_1\text{-}[0-8]$	3.7	3.7	3.7	3.7	
$\overline{E}_3\text{-}[0-8]$	5.2	5.3	5.3	5.3	
$\overline{E}_1\text{-}[10-25]$	15.2	15.2	14.8	14.9	
$\overline{E}_3\text{-}[10-25]$	15.9	16.0	15.6	15.8	
$E_{peak}$	2.7	2.7	2.7	2.7	
	10.3	10.3	10.3	10.2	
	14.3	13.4	13.6	13.2	
	16.9	18.0		17.9	$\overline{E} = 15.4$ [67]
					$\Gamma = 4.89$ [67]
% EWSR	%	%	%	%	%
[0 – 40]	99.0	101.5	97.2	99.6	
[0 – 8]	1.3	1.3	0.8	0.8	
[8 – 20]	85.7	80.6	81.4	78.1	
[13 – 18]	66.1	55.3	57.1	47.8	62 ( $\gamma, x$ ) [59]

TABLE XI. Same as table IV for the GDR in  $^{120}\text{Sn}$ .

$^{120}\text{Sn} / 2^+$	RPA	(c)	(i)	Theory (c+i)	Experiment
$\overline{E}_1\text{-}[0-40]$	15.8	16.3	15.6	16.1	
$\overline{E}_3\text{-}[0-40]$	17.8	19.6	18.1	19.7	
$\overline{\Gamma}\text{-}[0-40]$	4.8(4.2)	6.1(5.7)	5.3(4.8)	6.3(6.0)	
$\overline{E}_1\text{-}[0-8]$	5.8	5.8	4.9	4.9	
$\overline{E}_3\text{-}[0-8]$	6.3	6.3	5.5	5.6	
$\overline{E}_1\text{-}[10-25]$	16.6	16.6	16.3	16.4	
$\overline{E}_3\text{-}[10-25]$	17.1	17.5	16.9	17.3	
$E_{peak}$	6.0	6.0	4.7	4.7	
		12.8		12.6	$\overline{E} = 13.3(0.3)$ [56] $\Gamma = 3.7(0.5)$ [56]
	16.6	15.6	15.7	15.5	
% EWSR	%	%	%	%	%
[0 – 40]	69.8	68.1	68.0	67.0	
[0 – 8]	2.7	2.7	2.2	2.3	
[8 – 20]	55.1	43.3	52.5	43.0	
[10 – 16]	40.0	38.4	41.5	38.3	$53 \pm 13$ (p,p') [47] $41 \pm 9$ ( $\alpha, \alpha'$ ) [56] $36 \pm 6$ ( $^{17}\text{O}+^{120}\text{Sn}$ ) [50]

TABLE XII. Same as table IV for the GQR in  $^{120}\text{Sn}$ .



$^{208}\text{Pb} / 0^+$	RPA	(c)	(i)	Theory (c+i)	Experiment
$\overline{E}_{1-[0-40]}$	15.3	16.1	15.0	15.7	
$\overline{E}_{3-[0-40]}$	16.5	18.5	16.8	18.6	
$\overline{\Gamma}_{-[0-40]}$	3.4(2.5)	4.9(4.4)	4.0(3.3)	5.3(4.7)	
$\overline{E}_{1-[0-20]}$	14.6	14.4	14.0	13.9	
$\overline{E}_{3-[0-20]}$	15.0	14.9	14.5	14.5	
$\overline{\Gamma}_{-[0-20]}$	2.2(1.4)	2.4(1.8)	2.2(1.5)	2.4(1.9)	
$E_{peak}$	16.3	14.2	13.9	13.6	$\overline{E} \simeq 13.6$ [1,48] $\Gamma \simeq 2.5$ [1,48]
% EWSR	%	%	%	%	%
[0 – 40]	99.2	102.6	96.8	100.1	
[0 – 20]	88.5	70.7	75.9	65.8	
[10 – 16]	66.0	58.4	68.8	59.0	$63 \pm 17$ (p,p') [47] $64 \pm 13$ ( $\alpha, \alpha'$ ) [56] $61 \pm 13$ ( $\alpha, \alpha'$ ) [49] $59$ ( $\alpha, \alpha'$ ) [60] $69$ (p,p') [61] $64$ ( $^3\text{He}, ^3\text{He}$ ) [62] $84 \pm 30$ ( $^{17}\text{O} + ^{208}\text{Pb}$ ) [63] $92 \pm 8$ ( $^{17}\text{O} + ^{208}\text{Pb}$ ) [50]

TABLE XIII. Same as table IV for the GMR in  $^{208}\text{Pb}$ .

$^{208}\text{Pb} / 1^-$	RPA	(c)	(i)	Theory (c+i)	Experiment
$\overline{E}_{1-[0-40]}$	13.2	13.7	12.8	13.3	
$\overline{E}_{3-[0-40]}$	15.3	16.8	15.9	17.0	
$\overline{\Gamma}_{-[0-40]}$	4.2(3.5)	5.2(4.7)	4.9(4.3)	5.6(5.1)	
$E_{peak}$	2.1	2.1	2.1	2.1	
	13.0	12.5	11.6	11.4	
	16.7	16.7	16.7	16.7	$\overline{E} = 13.5$ [67]
					$\Gamma = 4.0$ [67]
% EWSR	%	%	%	%	%
[0 – 40]	99.2	101.8	95.9	97.2	
[0 – 5]	0.1	0.1	0.1	0.1	
[5 – 15]	70.7	59.8	65.0	59.2	
[15 – 25]	23.9	32.3	23.2	28.0	
[10 – 17]	75.5	66.0	66.1	61.0	68 ( $\gamma, x$ ) [64]
					91 ( $\gamma, x$ ) [65]
					90 ( $\gamma, x$ ) [66]
					68 (p,p') [61]

TABLE XIV. Same as table IV for the GDR in  $^{208}\text{Pb}$ .

$^{208}\text{Pb} / 2^+$	RPA	(c)	(i)	Theory (c+i)	Experiment
$\overline{E}_1\text{-}[0-40]$	11.5	12.4	11.2	12.0	
$\overline{E}_3\text{-}[0-40]$	14.6	17.6	15.4	18.0	
$\overline{\Gamma}\text{-}[0-40]$	4.9(4.4)	6.6(6.4)	5.6(5.2)	7.0(6.8)	
$\overline{E}_1\text{-}[8-20]$	13.2	13.0	12.5	12.6	
$\overline{E}_3\text{-}[8-20]$	13.5	13.9	13.0	13.6	
$\overline{\Gamma}\text{-}[8-20]$	1.7(1.1)	2.8(2.6)	1.9(1.5)	2.8(2.7)	
$\overline{E}_1\text{-}[0-8]$	5.1	5.1	4.4	4.4	
$\overline{E}_3\text{-}[0-8]$	5.9	5.9	5.1	5.1	
$\overline{\Gamma}\text{-}[0-8]$	1.8(1.6)	1.8(1.6)	1.6(1.2)	1.6(1.2)	
$E_{peak}$	6.2	6.1	4.9	4.8	
	13.0	11.2	12.1	10.8	$\overline{E} = 10.9$ [56]
		13.8		13.8	$\Gamma = 2.4(0.4)$ [56]
% EWSR	%	%	%	%	%
[0 – 40]	92.4	93.4	89.0	90.6	
[0 – 8]	10.7	10.5	9.2	9.1	
[8 – 12.5]	15.5	25.2	39.0	27.5	$49 \pm 12$ (p,p') [47] $44 \pm 10$ (p,p') [68] $44 \pm 8$ (p,p') [69] $62 \pm 11$ (p,p') [61] $50 \pm 8$ (O+Pb,H-I) [63] $50 \pm 5$ ( $\alpha, \alpha'$ ) [56] $33 \pm 8$ ( $^{17}\text{O}+^{208}\text{Pb}$ ) [50] $36 \pm 9$ ( $^{20}\text{Ne}+^{208}\text{Pb}$ ) [51]

TABLE XV. Same as table IV for the GQR in  $^{208}\text{Pb}$ .

(e,e') [2]	(p,p') [61]	(p,p') [3]	(c+i)	(c)	(i)
8.9	8.9	8.9			
9.4	9.3	9.4	9.3	9.3	9.3
9.6		9.6	9.9	9.9	
10.1		10.1	10.2	10.3	
10.7	10.6	10.7	10.7	10.8	
11.5		11.0	11.0	11.3	
					11.9

TABLE XVI. Experimental energies of peaks position observed in the GQR of  $^{208}\text{Pb}$  in (p,p') and (e,e') experiments. Calculated peak positions including the coherent, the incoherent and the coherent plus incoherent self-energies are reported under columns indicated by (c), (i) and (c+i), respectively.